# Prospect for detecting magnetism of a single impurity atom using electron magnetic chiral dichroism

Devendra Negi, Paul M. Zeiger, Lewys Jones, Juan-Carlos Idrobo, Peter A. van Aken, and Ján Rusz

Phys. Rev. B **100**, 104434 — Published 26 September 2019

DOI: 10.1103/PhysRevB.100.104434

# Prospect for detecting magnetism of a single impurity atom using EMCD

Devendra Negi,[1,2,*] Paul M. Zeiger,[2] Lewys Jones,[3,4] Juan-Carlos Idrobo,[5] Peter A. van Aken,[1] and Ján Rusz[2,†]

[1] *Stuttgart Center for Electron Microscopy, Max Planck Institute for Solid State Research, Heisenbergstr.1, 70569 Stuttgart, Germany*
[2] *Department of Physics and Astronomy, Uppsala University, P.O. Box 516, 75120 Uppsala, Sweden*
[3] *Advanced Microscopy Laboratory, Centre for Research on Adaptive Nanostructures and Nanodevices (CRANN), Dublin 2, Ireland*
[4] *School of Physics, Trinity College Dublin, Dublin 2, Ireland*
[5] *Center for Nanophase Materials Sciences, Oak Ridge National Laboratory, Oak Ridge, Tennessee 37831, USA*

(Dated: September 10, 2019)

Dopants, even single atoms, can influence the electrical and magnetic properties of materials. Here, we demonstrate the opportunity for detecting the magnetic response of an embedded magnetic impurity in a nonmagnetic host material. We combine a depth sectioning approach with electron magnetic circular dichroism (EMCD) in scanning transmission electron microscopy (STEM), to compute the depth-resolved magnetic inelastic scattering cross-section of single Co impurity buried in the host crystal of GaAs. Our calculations suggest that the magnetic dichroic signal intensity is sensitive to the depth and lateral position of the electron probe relative to the magnetic impurity. Additionally, a more precise dichroic signal localization can be achieved via choosing higher collection angle ($\beta$) apertures. Quantitative evaluation of the inelastic scattering cross-section and signal-to-noise ratio indicates that the magnetic signal from a single Co atom is on the verge of being detectable with today's state-of-the-art instrumentation.

## I. INTRODUCTION

The rise of the knowledge and data economy demands novel techniques and materials for both higher data processing and storage capability. The quest towards the ultimate data storage limit drives scientific investigation towards controlling and manipulating single atom magnets [1–5]. In pursuit of ultra-dense storage and efficient computation capability, quantum computing has attracted significant attention. Quantum computing utilizing a single atomic spin as a quantum qubit is envisaged as one of the most viable solutions [6–8]. In order to understand, manipulate and control atomic spins in the quantum regime, the ability to measure magnetic properties with atomic level sensitivity will be essential. Necessarily, detecting these properties in the quantum regime requires a probe of atomic size and sensitivity.

Previous works utilizing scanning tunneling microscope (STM) have captured the magnetic response of magnetic impurities at free surfaces and began a paradigm shift in atomically sensitive surface magnetic measurements [9–11]. More recently, the spin information of an atom on a surface was detected by utilizing the magneto-Seebeck effect. Such investigations further promise routes to energy efficient data processing [12]. Although, STM based detection methods are promising, they are restricted only to the surface of a material, and experience further challenges due to the poor surface stability of adatoms. In pursuit of robust and more dense memory storage, three dimensional (3D) atomic magnetic detection and manipulation capability would certainly lead to a manifold increment in storage capability [13]. A technique capable of providing atom-by-atom information will certainly be crucial in realizing any 3D magnetic detection.

In the context of 3D atomic scale magnetic measurements, electron beams in scanning transmission electron microscopy (STEM) can be focused into a sub-Ångström probe with current state-of-art instruments [14]. Although some existing techniques e.g., spin polarized tunneling electron microscopy [15, 16], x-ray magnetic circular dichroism (XMCD) [17, 18] are capable of rendering magnetic information with nano-scale precision, each of these techniques are also only surface sensitive and lack sufficient depth resolution. STEM, however, offers promising possibilities to overcome these limitations, with atomic scale imaging and spectroscopy are becoming increasingly common. For instance, recently deep sub-Ångström spatial resolution was successfully demonstrated in 2D materials utilizing electron ptychography [19]. On the other hand, the depth dependent information can also be retrieved in STEM, by combining the normal lateral scanning with a depth-sectioning (through focal series) approach.

Various investigations have unraveled 3D information with depth sectioning in STEM [14, 20–25]. For instance, a single buried Hf atom was imaged with nanometer precision by combining depth sectioning and Z-contrast imaging techniques[26]. Dislocations at a certain depth were also imaged by depth sectioning [27]. Furthermore, depth sectioning is indeed a promising approach from the perspective of three dimensional imaging in STEM [28–31], but it lacks so far of applications in the field of magnetism.

In order to retrieve depth-dependent magnetic information, an atomic-size probe is required, a sample thin enough to be electron transparent, and a detection strategy sensitive to magnetic interaction. These criteria are met by the electron probe and the electron magnetic chiral dichroism (EMCD) technique in aberration cor-

rected STEM. EMCD is based on electron energy-loss spectroscopy (EELS) and has gained significant attention since its first experimental demonstration [32–41]. Furthermore, EMCD sum-rules enable the quantitative determination of spin and orbital magnetic moments [42, 43]. Progress in EMCD is constantly pushing the spatial limits of magnetic detection towards atomic level [44]. In the most recent development of EMCD, magnetic dichroism has been imaged with atomic scale precision [45].

Although EMCD is quite promising for nano- and atomic-scale magnetometry, the weak cross-section for the underlying interaction means it suffers from low signal-to-noise ratios (SNRs). Enhancing magnetic signal to obtain higher magnetic SNR remains a key challenge in EMCD. Recent efforts in EMCD have been dedicated to enhancing the signal-to-noise ratio with novel signal collection strategies [46]. Detecting the magnetic response from a single magnetic atom will certainly pose a grand challenge for the ultimate capability of EMCD. It is noteworthy that by utilizing depth-resolved core-loss spectroscopy the feasibility of detecting a single embedded impurity in a host matrix was well proven by a theoretical study [47] and was subsequently demonstrated experimentally [48]. Such an approach is often termed energy-loss scanning confocal electron microscopy (SCEM).

In a previous paper we have computationally studied the feasibility of magnetic depth sectioning using electron vortex beams (EVBs) in STEM [14], evaluating the magnetic response of an Fe interlayer sandwiched in GaAs. An EVB was chosen as the probe, because it was determined to offer the strongest EMCD signal per electron dose in the atomic resolution regime [49]. Such theoretical insights are essential in aiming for the ultimate detection of a single magnetic impurity in a material. Although the experimental feasibility of this present proposal hinges on advanced techniques and instrumentation, there are nevertheless encouraging recent developments in the generation of electron vortex beams [50–53], detection strategies [46, 54], and other instrumental developments [55, 56]. All of these factors bring the possibility of detecting a single magnetic atom closer than ever before.

In this work we quantitatively evaluate the inelastic scattering cross-section of a single Co atom implanted at a certain depth in a GaAs host matrix. Our calculations illustrate the intensity of the magnetic response as a function of the lateral and depth proximity of the probe focus and the magnetic impurity, see Fig. 1. The remainder of this manuscript is structured as follows; section II describes the method of quantitatively calculating the inelastic scattering cross-section. In Sec. III, the magnetic and non-magnetic components of the inelastic scattering cross-sections are presented. Using this simulation framework, the focus of the probe is varied in the lateral and vertical directions, and the influence of the size of the collection angle is discussed. Quantitative evaluation of the magnetic SNR was also performed in order

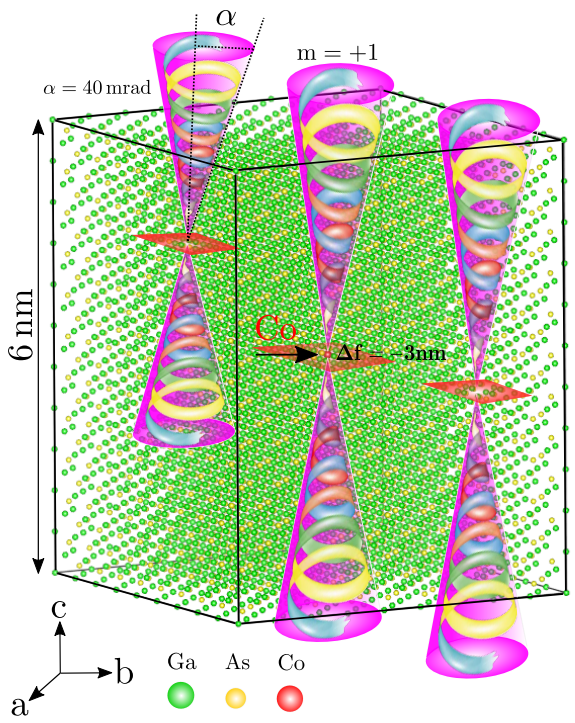


FIG. 1. Schematic illustration of the calculation methodology for depth sectioning by EMCD for a system with a single Co atom embedded in a non-magnetic GaAs host matrix. EVB probes can be shifted in lateral $(x, y)$ and vertical $(z)$ direction.

to estimate the experimental feasibility of the proposed measurement. Finally, Sec. IV summarizes our findings.

## II. METHODS

In this section, we describe the quantitative evaluation of the magnetic and non-magnetic components of the inelastic scattering cross-section and the corresponding electron-counts recorded for a given electron-dose incident on the sample.

### A. Inelastic scattering cross-section and detected electron counts

Calculation of the inelastic scattering cross-sections was performed using a combined multislice/Bloch-waves approach [57] as implemented in the MATS.v2 software [58]. These calculations are based on the first Born approximation formula

$$\frac{\partial^2\sigma}{\partial E\partial\Omega} = \frac{4\gamma^2}{a_0^2}\frac{k_{\rm out}}{k_{\rm in}}\sum_{\mathbf{a},\mathbf{q},\mathbf{q}'} A_{\mathbf{q},\mathbf{q}'}e^{i(\mathbf{q}'-\mathbf{q})\cdot\mathbf{a}}\frac{S(\mathbf{q},\mathbf{q}',E)}{q^2q'^2} \quad (1)$$

where $\sigma$ represents the scattering cross-section which is dependent on both the energy loss $E$ and scattering angle $\Omega$. Factors $\gamma$ and $a_0$ stand for the relativistic mass enhancement factor and Bohr radius, respectively. The wave-vector lengths $k_{\rm in}$ and $k_{\rm out}$ are the relativistically corrected de Broglie electron wave-lengths before and after the inelastic event. Element of spherical angle $\partial\Omega$ is centered around $\mathbf{k}_{\rm out}$ and defines the direction, with respect to which the momentum transfers $\mathbf{q}, \mathbf{q}'$ are calculated [57]. The sum runs over all magnetic atoms in the simulation cell across the thickness of the simulated material (positions $\mathbf{a}$) and over pairs of momentum transfer vectors $\mathbf{q}, \mathbf{q}'$, for which their complex amplitude $A_{\mathbf{q},\mathbf{q}'}$ has a modulus larger than a given cut-off. Determination of these terms and their amplitudes $A_{\mathbf{q},\mathbf{q}'}$ is the primary task of the MATS.v2 code. Finally, $S(\mathbf{q}, \mathbf{q}', E)$ stands for the mixed dynamical form-factor (MDFF, [59]).

In the dipole approximation, for isotropic materials magnetized along the $z$-direction, the MDFF can be written as [49]

$$S(\mathbf{q}, \mathbf{q}', E) = (\mathbf{q} \cdot \mathbf{q}')N(E) + i(\mathbf{q} \times \mathbf{q}')_z M(E), \qquad (2)$$

where $N(E), M(E)$ are determined by the electronic structure of the material. If one neglects the orbital magnetic moment, magnetic dipole term and the anisotropic orbital term [60, 61] in the sum rule expressions [42], one obtains the following approximation for the MDFF

$$S(\mathbf{q}, \mathbf{q}') \approx \frac{1}{45}\langle r\rangle^2[4N_h(\mathbf{q}.\mathbf{q}') + i\frac{m_S}{\mu_B}(\mathbf{q} \times \mathbf{q}')_z], \qquad (3)$$

where $\langle r\rangle$ is an integral over the radial parts of the initial $2p$ electron wave-function and the final $3d$ electron wave-function multiplied by $r$, which can be evaluated by density functional theory (DFT); this is discussed in the next subsection. Similarly, the number of holes in the $3d$ shell $N_h$ and the spin moment of the Co atom $m_S$, expressed in Bohr magnetons $\mu_B$, can be calculated using DFT.

By integrating the double-differential scattering cross-section over the $L_3$-edge and over a suitable range of scattering angles collected by the detector, we obtain for the non-magnetic ($\sigma_N$) and magnetic ($\sigma_M$) components of the total scattering cross-section the following expressions:

$$\sigma_N = \frac{16N_h\gamma^2\langle r\rangle^2}{45a_0^2}\frac{k_{\rm out}}{k_{\rm in}}\int_{\rm det.} d\Omega \sum_{\mathbf{a},\mathbf{q},\mathbf{q}'} A_{\mathbf{q},\mathbf{q}'} e^{i(\mathbf{q}'-\mathbf{q})\cdot\mathbf{a}} \frac{\mathbf{q}\cdot\mathbf{q}'}{q^2 q'^2} \qquad (4)$$

$$\sigma_M = \frac{4m_S\gamma^2\langle r\rangle^2}{45\mu_B a_0^2}\frac{k_{\rm out}}{k_{\rm in}}\int_{\rm det.} d\Omega \sum_{\mathbf{a},\mathbf{q},\mathbf{q}'} A_{\mathbf{q},\mathbf{q}'} e^{i(\mathbf{q}'-\mathbf{q})\cdot\mathbf{a}} \frac{i(\mathbf{q}\times\mathbf{q}')_z}{q^2 q'^2} \qquad (5)$$

An important advantage of these expressions lies in the complete separation of the electronic structure dependent part (the prefactor) from the dynamical diffraction dependent part (the sum), which can be thus calculated entirely independently. While MATS.v2 solves the dynamical diffraction part, DFT calculations provide the necessary inputs for the prefactor.

The conversion from the components of the inelastic scattering cross-section to electron counts is straightforward. Assume a beam current $I$ hitting the sample and a dwell time of $\Delta t$. The electron dose (number of electrons) irradiating the sample is $I\Delta t/e$, where $e > 0$ is an elementary charge. Due to periodic boundary conditions in lateral coordinates $x, y$, the predicted detected electron counts can be obtained as

$$N_{\rm mag} = \frac{I\Delta t}{e}\frac{\sigma_M}{S} \qquad \text{and} \qquad N_{\text{non-mag}} = \frac{I\Delta t}{e}\frac{\sigma_N}{S} \qquad (6)$$

where $S = ab$ is the lateral area of the supercell with lattice parameters $a, b, c$, assuming that the electron beam propagates parallel to the $c$-axis. In these expressions, the $\sigma_{M,N}/S$ represent the fraction of incoming electrons that get inelastically scattered into the detector aperture within the energy range of the Co $L_3$-edge. Note that while $N_{\text{non-mag}}$ is always positive, $N_{\rm mag}$ can also be negative. However, one cannot measure $N_{\rm mag}$ separately from $N_{\text{non-mag}}$, in comparison to which it is strictly smaller, because $m_S/\mu_B \leq N_h < 4N_h$ (see Eq. 3).

In this paper we considered an illuminating electron probe current of 100 pA and a dwell time of 50 ms for the evaluation of detected electron counts (Eq. 6). An atomic size coherent beam with current of 100 pA is achievable with today's state-of-the-art cold field emission guns [62]. What still remains a challenge is to create isolated atomic size vortex beam with enough current and maintaining coherence. Yet, reports using magnetized needle [63, 64], and lately programable phase plates [65] indicate that 100 pA vortices should be realizable with technology of today or of the near future. On the other hand, dwell times of 50ms/pixel for total acquisition times of few minutes in spectrum images are common in STEM-EELS experiments. The particular chosen value bears no special importance other than being on the higher end of the commonly used values. Eventually the resistance of the sample to the radiation damage will determine the practical dwell times in each experiment.

### B. Evaluation of radial integral using density functional theory

The method for evaluating the average radial integral $\langle r\rangle$ is similar to the evaluation of the radial integrals over Bessel functions given in the supplementary material of Ref. [32]. Focusing on the $L_{2,3}$ edges, the inelastic transitions from initial $2p$ states to final $3d$ states ($L = 2$) are considered. The final state wave-function depends on the energy $E$ above the Fermi level $E_{\rm F}$ and, assuming that it depends only weakly on $E$, $\langle r\rangle$ is computed as an average of radial integrals $\langle r\rangle_{EjLS}$ over an energy interval $\Delta E = [E_{\rm F}, E_{\rm F} + 20.0\text{ eV}]$,

$$\langle r\rangle = \frac{1}{\Delta E}\int_{\Delta E} \mathrm{d}E\ \langle r\rangle_{EjLS}, \qquad (7)$$

where $j \in \{\frac{1}{2}, \frac{3}{2}\}$ is the total angular momentum quantum number of the initial state and $S = \pm\frac{1}{2}$ the spin

quantum number. Strictly speaking $\langle r \rangle$ as defined here is dependent on $j$ and $S$ but the differences between the values for different combinations of $j$ and $S$ are below 3% and the average over the possible combinations of $j$ and $S$ is therefore taken to be a representative value of $\langle r \rangle$. The energy dependent radial integrals themselves read

$$\langle r \rangle_{EjLS} = \int \mathrm{d}r\, r^3\, R_{jS}(r)\, u_{ELS}(r). \tag{8}$$

Here $R_{jS}(r)$ and $u_{ELS}(r)$ are the radial parts of the initial and (energy-dependent) final state wave functions, respectively. Note that in the dipole approximation used in this work the radial integral is $q$-independent. That means, that the radial wavefunctions of the orbitals involved in the atomic excitation, influence the inelastic scattering cross-section only via an overall scaling factor $\langle r \rangle^2$, see Eqns. 4 and 5.

For the purposes of this semi-quantitative study, the value of $\langle r \rangle$ was calculated for the elemental hcp-Co crystal instead of using the large supercell of GaAs with a single Co impurity shown in Fig. 1. Combined LAPW+lo and APW+lo basis, as implemented by WIEN2k in version 14.2 [66], was used in the DFT calculations with a basis size cut-off value of $RK_{\max} = 8.0$. $R_{jS}(r)$ is then taken to be the radial part of the corresponding core wave function as computed by WIEN2k and $u_{ELS}(r)$ is calculated as a solution to the scalar relativistic Schrödinger equation incorporating the converged (spin-dependent) spherical potential as calculated by WIEN2k. The radial integral in Eq. 8 is performed up to the muffin-tin radius $R_{\mathrm{MT}} = 2.3\ a_0$. Following this procedure, a value of $0.139\ a_0$ is obtained for $\langle r \rangle$. The energy-dependent radial integral $\langle r \rangle_{EjLS}$ is a smoothly and slowly varying function of energy $E$. Its values vary within $\pm 10\%$ of the average $\langle r \rangle$ in the energy interval $\Delta E$, motivating the assumption of a weak energy dependence and thus taking the average according to Eq. 7 as a representative value for all $\langle r \rangle_{EjLS}$.

The same WIEN2k calculation yields for the $3d$-shell of Co a spin magnetic moment of $m_S \approx 1.7\ \mu_B$ and a value of $N_h = 2(2L+1) - [N_\uparrow + N_\downarrow] = 10 - N_e \approx 2.8$ for the number of holes. $N_e$ is thereby the total number of electrons in the shell, and $N_\uparrow$ and $N_\downarrow$ the corresponding numbers of electrons in the spin-up and spin-down channels, respectively.

### C. Dynamical diffraction calculations

Figure 1 shows a schematic diagram representing the calculation scheme. A single magnetic impurity in form of a Co atom is implanted in a GaAs block. GaAs is a technologically important semiconductor material and serves as a nonmagnetic host in this case study. It has a cubic structure with lattice parameter of 5.65 Å. In our simulation study, a 6 nm thickness of GaAs, oriented in [001] zone axis is considered as the host material, and one Ga atom was substituted with a Co atom at $\sim 3$ nm depth. The Co atom was implanted at the center of the $(3 \times 3 \times 11)$ supercell of GaAs with dimensions $a = b = 16.95$ Å and $c = 62.15$ Å, thus $S = ab = 287.3$ Å$^2$. Such a supercell contains 792 atoms in total.

The acceleration voltage of the electron microscope was set to 200 kV. A typical aberration-corrected convergence semi-angle of 40 mrad was considered for the convergent EVB probe with orbital angular momentum of $+1\hbar$. In the multislice calculations the cell was further extended $(3 \times 3 \times 1)$ times in $(x, y, z)$ directions to minimize overlap of the probe with its periodic images. Calculations were carried out by varying the defocus from $\Delta f = -0.5$ nm to $\Delta f = -6.0$ nm in steps of $\Delta f = -0.5$ nm. Zero defocus puts the focal plane on the entrance surface of the sample and negative $\Delta f$ represents an underfocus, moving the focal plane deeper inside the sample. The differential scattering cross-section was evaluated on a grid of scattering angles ranging from $-25$ mrad to $+25$ mrad in both scattering directions, $\theta_x, \theta_y$, with a step of 2 mrad. The influence of lateral and vertical proximity of the probe focus to the impurity column was calculated by shifting the probe in $x$ ($\Delta X$) and $z$ ($\Delta f$) directions. The total scattering cross-section was calculated by integrating the differential scattering cross-section over on-axis circular detectors of radii $5-25$ mrad corresponding to a choice of different spectrometer collection apertures. The convergence parameter in MATS.v2 was set to $5 \times 10^{-7}$.

## III. RESULTS AND DISCUSSION

### A. Dichroic signal distribution

Figure 2 (a) shows the distribution of the magnetic dichroic signal within the calculated range of scattering angles for various defocus values and probe distances from the atomic column containing Co atom. The range of calculated $\Delta f$ covers the entire thickness of the material. The peak value of the differential scattering cross-section is obtained at $\Delta f = -2$ nm and $\Delta X = 0$. The differential scattering cross-section is integrated over the energy loss range covering the Co-$L_3$ edge.

In the top row, the EVB is passing directly through the atomic column containing the magnetic impurity. The magnetic dichroic signal is uniformly distributed around the center of calculated grid of scattering angles. The intensity of the dichroic signal increases progressively as the defocus approaches the depth of the magnetic impurity. It is intriguing to observe that the dichroic intensity attains maximum values around $\Delta f = -2$ nm, while the magnetic impurity is located at the depth of 3 nm (i.e., corresponding defocus would be $\Delta f = -3$ nm). Note also the widening of the magnetic signal distribution as a function of scattering angles, as the defocus moves the beam waist closer to the Co atom. The intensity of the magnetic dichroic signal quickly vanishes by moving the focal plane away from the location of the Co atom.

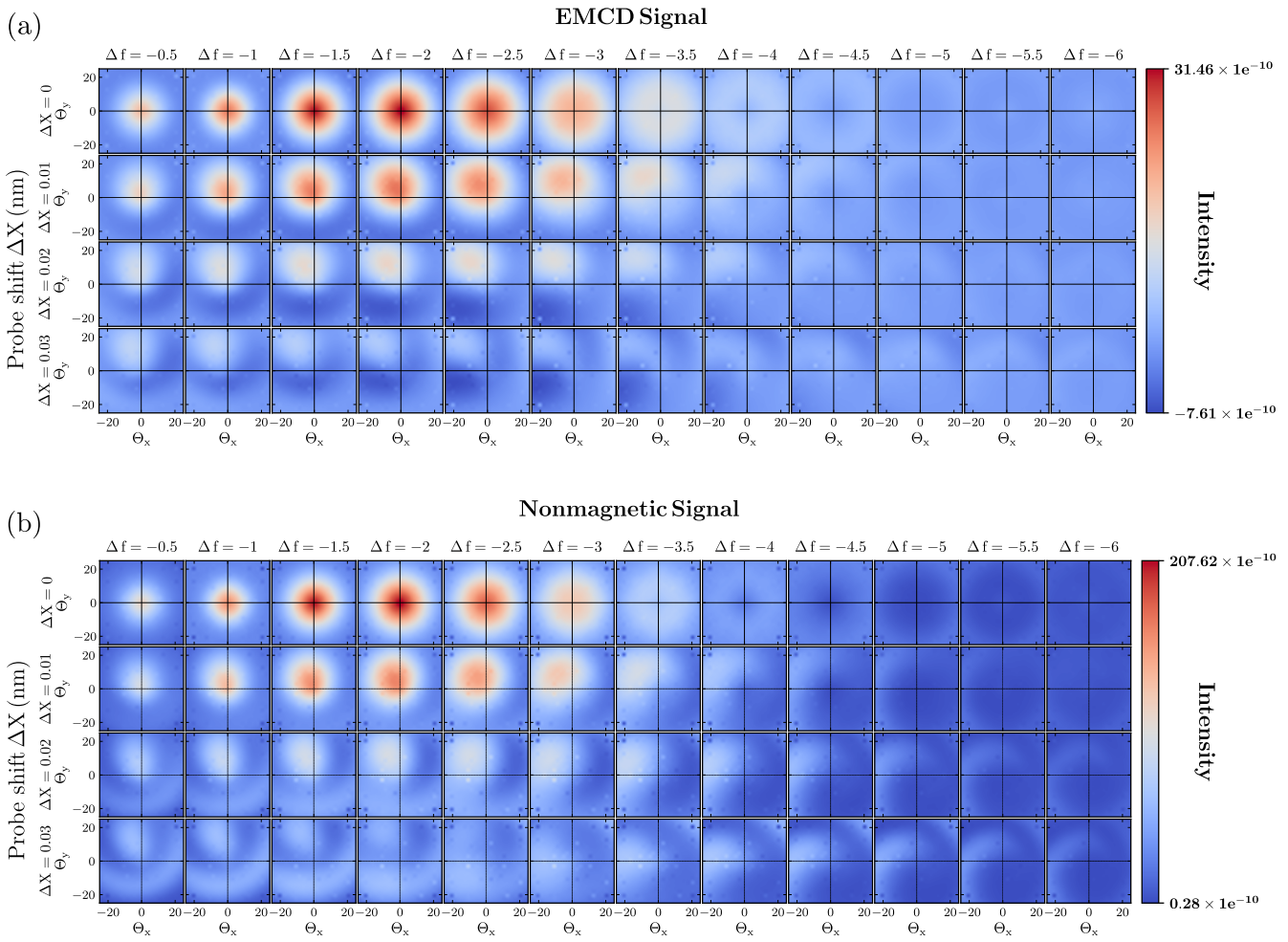


FIG. 2. Evolution of (a) magnetic ($\sigma_M/S$) and (b) nonmagnetic ($\sigma_N/S$) signal with varying defocus $\Delta f$ (nm) and the probe shift $\Delta$X (nm) from the atomic column containing magnetic impurity. Each panel spans a range of scattering angles $\Theta_x, \Theta_y$ from $-25$ to $+25$ mrad. Scattering cross-sections are discretized over a spherical angle of 4 mrad$^2$, corresponding to pixel size in the diffraction patterns.

The relation of maximum dichroic signal and optimized $\Delta f$ can be comprehended by the depth of focus ($\Delta z$).The depth of focus defines the vertical depth around the focal plane, within which the probe diameter remains less than the factor of $\sqrt{2}$ larger than the beam waist. $\Delta z$ proportionally depends on the probe wave length ($\lambda$) and inverse proportionally to the square of the convergence semi-angle ($\alpha$), and is given by the relation $\Delta z = \frac{1.77\,\lambda}{\alpha^2}$ [47]. In the present calculation, these parameters are $\alpha = 40$ mrad and $\lambda(\mathrm{V_{acc}} = 200\,\mathrm{kV}) \approx 2.51$ pm and the depth of focus is thus $\Delta z \approx 2.7$ nm. Therefore, the imprecision of depth-location of the impurity atom is safely within an expected error range of $\sim \frac{\Delta z}{2}$.

The nonmagnetic signal distribution follows qualitatively the footprint of the EMCD signal distribution, see top line of Fig. 2(b). As for the magnetic signal, also the nonmagnetic component of the inelastic scattering cross-section maximizes at the focal plane 1 nm above the Co atom. Note, however, that we discuss the peak values of the differential scattering cross-section here. Integration over a range of scattering angles may lead to a different picture due to widening of the signal in the diffraction pattern as the focal plane approaches the location of Co atom, see Sec. III B.

Next we focus on the EMCD signal distribution as a function of the lateral proximity ($\Delta$X) of the probe to the magnetic impurity. In Fig. 2(a), rows 2–4 show the EMCD signal distribution while shifting the probe progressively away from the atomic column, containing the magnetic impurity. Compared to the dependence on defocus parameter, the dichroic signal intensity reduces more rapidly as $\Delta X$ increases. This is a consequence of depth of focus being over an order of magnitude larger than the beam waist. Using the Rayleigh criterion for

the definition of the beam diameter at the beam waist one obtains $0.61\lambda/\alpha = 0.038$ nm. Shifting the probe by 0.02 nm, which is approximately the size of the probe radius, leads to a significant decrease of the inelastic scattering cross-section. When setting $\Delta f \approx 2.5$ nm, the maximum EMCD signal intensity retains $\sim 70\%$ at the nearest probe shift (0.01 nm), whereas, setting the location of the probe at $\sim 0.03$ nm away from Co atomic column, the maximum dichroic signal intensity remains below 10% of the maximum EMCD signal. The distribution of the magnetic signal in the diffraction plane becomes gradually more distorted as the probe focus is moved away from the Co atom.

The qualitative analysis presented so far has discussed the dependence of the EMCD and nonmagnetic signal on scattering angles, and further outlined the influence of vertical and lateral proximity of the electron probe focus to the embedded magnetic impurity. Although the computational results are encouraging, a successful measurement will hinge on the available state-of-art TEM instrumentation [55, 56, 67], because the detection of single atom magnetism via EMCD is expected to be extremely challenging due to the limited number of detectable electron counts. Therefore, before undertaking such an experiment, it would be imperative to have prior information at hand about the approximate depth and lateral location of embedded magnetic impurities. One approach could be to detect the core loss (Co-$L_{3,2}$) spectra as a function of $\Delta f$. Previously, it has been shown that such an approach can also provide a rough estimation of the thickness of the specimen at hand [68]. The intensity of the characteristic core loss signal will be maximized at the depth of the embedded impurity. Therefore, a through-focal series core loss (Co-$L_{3,2}$) experiment would provide a valuable quick estimation of the location of the magnetic atom [47, 48]. Alternatively such information can also be retrieved via careful $Z$-contrast imaging, under the condition of a sufficient relative mass difference between the dopant and the host crystal to enable discernible contrast differences [26]. The next step can be a fine tuning of $\Delta f$ to obtain the most probable depth location of the magnetic atom, for maximizing the signal intensity. Such method can also be useful for detecting certain magnetic layers in heterostructures or magnetic multilayer systems. For determining the probable lateral location of the magnetic impurity, the process mentioned above can be repeated across a 2D raster scan. The necessary electron dose is another key factor crucial in obtaining sufficient signal intensity while minimising unwanted radiation damage. Recently such challenges were tackled to maximize the signal-to-noise ratio while minimizing damage of the sample by the electron beam [69].

### B. Magnetic depth-sectioning

The EMCD and nonmagnetic signal distribution at various scattering angles as a function of $\Delta f$ and probe displacement from the impurity column was presented in the previous section. This section will focus on optimizing the signal collection. Therefore the $\Delta f$-dependent magnetic and nonmagnetic electron counts (Eq. 6) as well as the resulting relative EMCD strength at a collection angle of $\beta = 25$ mrad are computed. $\beta$ is chosen such that the dichroic signal is enclosed within the calculated range of scattering angles.

Figure 3 shows the line plots which illustrate the $\Delta f$ dependent EMCD, nonmagnetic, and relative EMCD signals at various $\Delta X$. The EMCD and nonmagnetic signal maximize at $\Delta f = -2.5$ nm, whereas the maximum relative EMCD signal is achieved at $\Delta f = -3.5$ nm. Since the plots in Fig. 2 show that the magnitude of the nonmagnetic signal reduces more steeply than magnetic signal as the focal plane moves below the impurity location, the intensity of the relative EMCD signal keeps growing until $\Delta f = -3.5$ nm. Still, the optimal $\Delta f$ remains close to the location of the buried magnetic impurity, within the expected imprecision range of $\Delta z/2$ given by the depth of focus.

Moving the probe $\sim 0.01$ nm away from the atomic column containing the magnetic impurity shows similar trends in the EMCD and nonmagnetic signal profiles. However, shifting the probe a bit further away from the Co column ($\Delta X = 0.02$ nm), a distinct trend can be observed in the EMCD signal. The EMCD signal drastically reduces and remains below approximately 15% of the maximum EMCD signal. In the extreme case, when the probe is displaced by a distance $\Delta X \approx 0.3$ nm away from the impurity column, the EMCD signal falls into the negative regime. Interestingly, the maximum amplitude of the magnetic signal remains at $\Delta f = -2.5$ nm.

Overall, it is interesting to see that the optimum of the scattering cross-section (i.e., integral of differential scattering cross-section over the detector aperture) is observed at a focal plane closer to the impurity atom than the calculated optimal value of the differential scattering cross-section discussed in the previous section. A more detailed dependence of the scattering cross-section on the collection angle will be presented in the next section.

### C. Signal collection

This section explores the dependence of the predicted electron counts on the collection semi-angle $\beta$ and displacement of probe focus from the Co atom. Figure 4 summarizes the results for different collection angles. The predicted magnetic and non-magnetic electron counts, Eq. 6, the relative strength of magnetic signal and a semi-quantitative estimation of the SNR as $2N_{\text{mag}}/\sqrt{2N_{\text{non-mag}}}$ are presented. The latter is an upper limit estimate, assuming that the power-law background

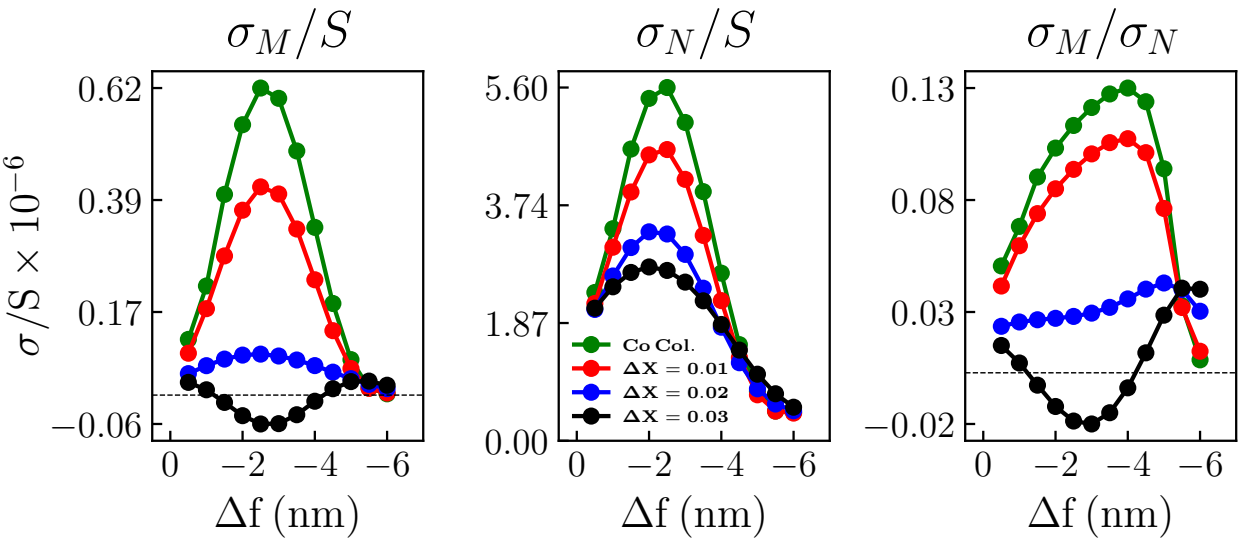


FIG. 3. Depth-dependence of (a) magnetic ($\sigma_M/S$) and (b) non-magnetic ($\sigma_N/S$) components of the scattered electron fraction for a collection semi-angle of $\beta = 25$ mrad. $\sigma_{N,M}$ are non-magnetic and magnetic components of inelastic scattering cross-section (Eqns. 4 and 5) and $S$ represents lateral area of simulation supercell, see Sec. II A for details. (c) Relative strength of EMCD signal ($\sigma_M/\sigma_N$). Different curves correspond to different distances $\Delta X$ of the beam from the atomic column containing Co impurity atom.

is negligible compared to the intensity of the Co-$L_{2,3}$ white lines. In Refs. [49, 70, 71] a more precise estimate suggests that an additional factor of $1/\sqrt{1+b}$ should be added to consider the background counts, where $b$ is the ratio of the energy-integrated background to the Co $L_3$-edge counts. Factors of 2 in the SNR expression come from an assumption that the magnetic signal is extracted as a difference of two measurements of inelastic scattering cross-sections, which have the same non-magnetic component, while the magnetic one changes sign. This can be achieved by changing the sign of the orbital angular momentum of the electron beam.

Figure 4 indicates that a higher accuracy in the localization of the impurity atom can be achieved by using a larger collection aperture: by increasing the collection angle, the optimal $\Delta f$ value approaches the depth location of the magnetic impurity from above. Our results show an agreement with previous reports, which studied the core-loss SCEM and advocated the requirement of higher probe convergence and collection aperture for achieving a more localized signal from the single impurity embedded in GaAs [47, 48], and with our previous work, where the optimal defocus was as well found to be located above the magnetic layer [14]. Qualitatively one can explain the observation that the optimal defocus might be different from the location of the impurity in the following way: At lower collection angles a significant fraction of detected inelastically scattered electrons originates from beam electrons, which hit the sample under (near-)zone-axis orientation. These electrons are subjected to dynamical diffraction effects more strongly than electrons that hit the sample under larger inclination angles. Such dynamical effects could explain reduced precision of the atom localization for small collection angles. As the collection angle increases, the weight of the more inclined beam electrons (which are less diffracted by lattice) in the scattering cross-section increases. With reduced impact of dynamical diffraction effects, the precision of atom localization improves.

As a function of $\Delta f$, the appreciable EMCD and non-magnetic counts span $\sim \pm 1$ nm from the maximal value. The relative EMCD signal strength as a function of $\Delta f$ and $\Delta X$ shows a rather different pattern. For lower collection angles ($\beta$ between 5–15 mrad), the relative EMCD signal persists from $\Delta f = -0.5$ to $\Delta f = -4.5$ nm, whereas at higher collection angles (20 – 25 mrad) it stretches from $\Delta f = -1$ to $\Delta f = -5$ nm. At higher collection angles, the relative EMCD signal approaches the trend of the EMCD signal and tends to localize around the embedded magnetic impurity. For $\beta$ in the range 5–20 mrad, the intensity of the relative EMCD signal maximizes for $\Delta f$ very close to the depth location of Co atom. However, at higher collection angles (25 mrad) the maximum intensity of the relative EMCD signal is found about 1 nm deeper than the position of Co atom.

As a function of lateral probe shift, the relative EMCD signal is centered on the atomic column containing the Co atom. At lower collection angles, the nonzero relative dichroic signal persists from the surface down to greater depth. In an earlier report it was suggested that while

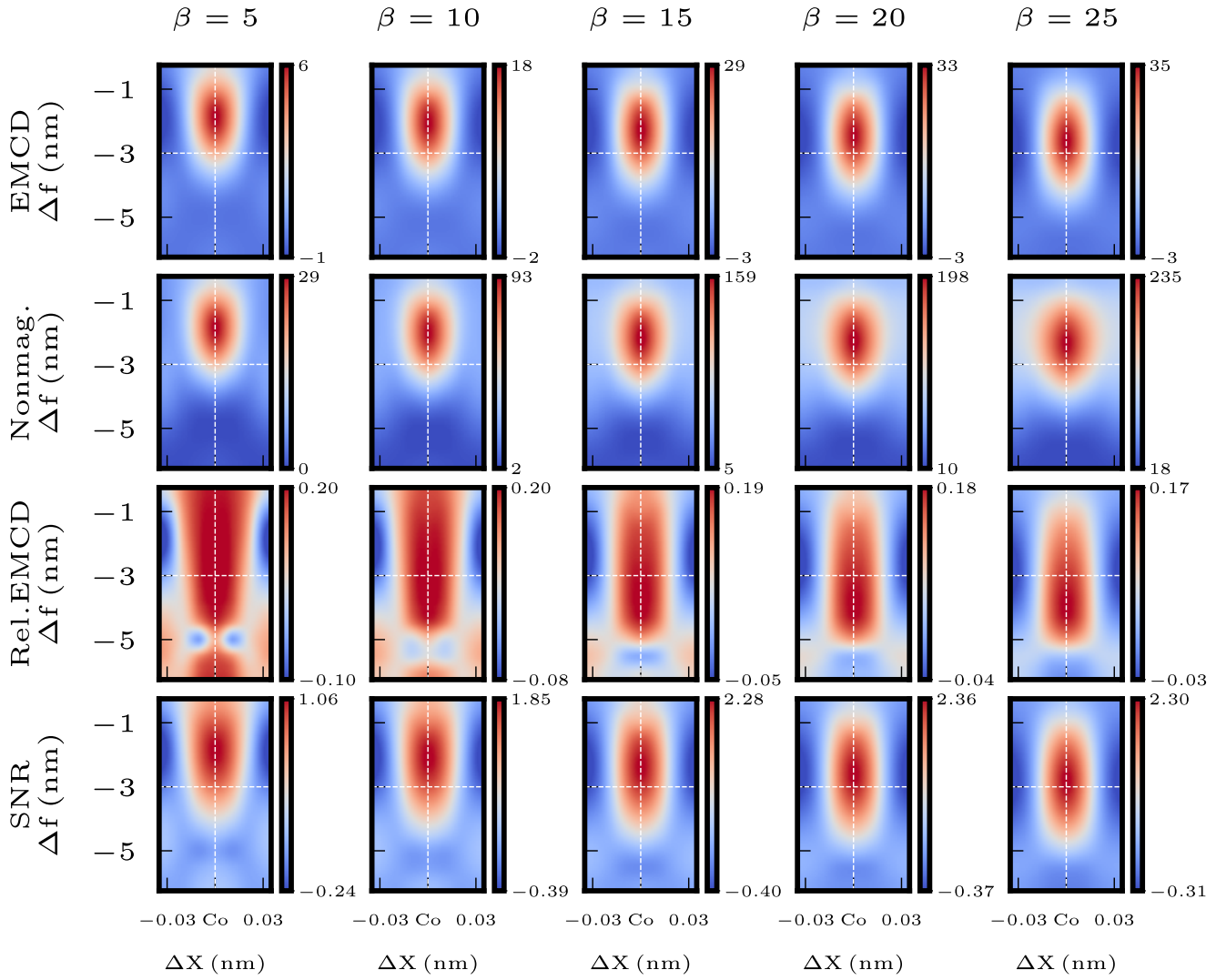


FIG. 4. Depth-resolved magnetic and nonmagnetic electron counts, relative EMCD strength and magnetic SNR for all defoci ($\Delta f$) and probe shifts from the Co impurity column ($\pm\Delta X$) evaluated at various collection semi-angles ($\beta$ = 5–25 mrad).

the probe is focused on the surface and if it couples to 1$s$-like Bloch state, then a subsequent channeling along the column can exert the ionization even at the impurity depth [47]. However, at higher collection angles such channeling is necessarily less effective.

The behavior of the SNR is qualitatively similar to the EMCD counts. As the collection angle is increased, the peak of the SNR approaches the position of the impurity atom. From a practical perspective, the predicted values of the SNR are very important, because they should determine how realistic it is to perform such an experiment. For a beam current of 100 pA and a dwell time of 50 ms the maximal SNR values approach a value of approximately 2.5. Such value does not allow for unambiguous detection of the EMCD signal per scan point. Moreover, this value assumes pure Poisson noise, i.e., achievable only with direct electron detectors. Furthermore, the background signal will decrease the SNR by a factor of $1/\sqrt{1+b}$ as discussed above, bringing it deeper below three. On the other hand, with increase of the beam current, the dwell-time, or by using frame summing [72], SNR values above three should be achievable. We conclude this analysis by noting that our simulations suggest that the detection of EMCD from a single magnetic impurity is near the edge, or rather slightly beyond the present technical possibilities. Nevertheless, with improvements of instrumentation, e.g., using high brightness electron guns and direct electron detectors, supported by advanced data post-processing methods [73], capable of taking an advantage of correlations of datasets with neighboring $\Delta f$ and $\Delta X$ values, the realization of such an experiment is not out of reach.

## IV. OUTLOOK AND CONCLUSIONS

We have computationally explored the feasibility of detecting the magnetic response of a single magnetic impurity embedded in a nonmagnetic host material. We combine an optical depth sectioning approach with EMCD in STEM to detect the magnetic response of a single Co atom, buried in nonmagnetic GaAs host material. The intensity of the depth resolved magnetic component of the inelastic cross-section of the Co atom in GaAs is sensitive to the lateral and depth proximity of the probe focus to the embedded Co atom. In the lateral direction, the magnetic signal practically disappears for shifts comparable to the size of the beam waist, while in the vertical direction, the determining parameter is the depth of focus. The precision of localization of the impurity atom improves for larger collection angles.

Our simulations, as a proof of concept study, affirm the viability of the ultimate limit of three-dimensional magnetic measurements in STEM, placing the predicted signal to noise ratios at the verge of detectability. The present proposal certainly poses significant challenges from the perspective of the experimental realization, yet, current advances in STEM instrumentation are bound to surpass such challenges. Successful realization of such an experiment has the potential to revolutionize our understanding of magnetism.

## ACKNOWLEDGMENTS

D. S. Negi, J. Rusz and P. M. Zeiger acknowledge funding from Swedish Research Council, Göran Gustafsson's foundation and Swedish National Infrastructure for computing (SNIC) at the NSC center (computer cluster Tetralith). This research was also supported by the Center for Nanophase Materials Sciences, which is a Department of Energy Office of Science User Facility (J.C.I.). This project has received funding from the European Unions Horizon 2020 research and innovation programme under grant agreement No. 823717 ESTEEM3.

* D.Negi@fkf.mpg.de
† jan.rusz@physics.uu.se

[1] K. Yang, W. Paul, F. D. Natterer, J. L. Lado, Y. Bae, P. Willke, T. Choi, A. Ferrón, J. Fernández-Rossier, A. J. Heinrich, and C. P. Lutz, Phys. Rev. Lett. **122**, 227203 (2019).
[2] F. D. Natterer, K. Yang, W. Paul, P. Willke, T. Choi, T. Greber, A. J. Heinrich, and C. P. Lutz, Nature **543**, 226 (2017).
[3] P. Gambardella, S. Rusponi, M. Veronese, S. Dhesi, C. Grazioli, A. Dallmeyer, I. Cabria, R. Zeller, P. Dederichs, K. Kern, *et al.*, Science **300**, 1130 (2003).
[4] S. Yan, D.-J. Choi, J. A. Burgess, S. Rolf-Pissarczyk, and S. Loth, Nano Letters **15**, 1938 (2015).
[5] R. Ishikawa, A. R. Lupini, S. D. Findlay, T. Taniguchi, and S. J. Pennycook, Nano Letters **14**, 1903 (2014).
[6] A. Heinrich, J. Gupta, C. Lutz, and D. Eigler, Science **306**, 466 (2004).
[7] Y.-C. Lin, P.-Y. Teng, P.-W. Chiu, and K. Suenaga, Physical Review Letters **115**, 206803 (2015).
[8] T. D. Ladd, F. Jelezko, R. Laflamme, Y. Nakamura, C. Monroe, and J. L. OBrien, Nature **464**, 45 (2010).
[9] A. A. Khajetoorians and A. J. Heinrich, Science **352**, 296 (2016).
[10] F. Donati, S. Rusponi, S. Stepanow, C. Wäckerlin, A. Singha, L. Persichetti, R. Baltic, K. Diller, F. Patthey, E. Fernandes, *et al.*, Science **352**, 318 (2016).
[11] F. D. Natterer, F. Donati, F. Patthey, and H. Brune, Physical Review Letters **121**, 027201 (2018).
[12] C. Friesen, H. Osterhage, J. Friedlein, A. Schlenhoff, R. Wiesendanger, and S. Krause, Science **363**, 1065 (2019).
[13] O. Ozatay, A. Gokce, T. Hauet, L. Folks, A. Giordano, and G. Finocchio, Physical Review Applied **11**, 014002 (2019).
[14] D. Negi, L. Jones, J.-C. Idrobo, and J. Rusz, Physical Review B **98**, 174409 (2018).
[15] R. Wiesendanger, I. Shvets, D. Bürgler, G. Tarrach, H. Güntherodt, J. Coey, and S. Gräser, Science **255**, 583 (1992).
[16] S. Heinze, M. Bode, A. Kubetzka, O. Pietzsch, X. Nie, S. Blügel, and R. Wiesendanger, Science **288**, 1805 (2000).
[17] X. Zhu, A. P. Hitchcock, D. A. Bazylinski, P. Denes, J. Joseph, U. Lins, S. Marchesini, H.-W. Shiu, T. Tyliszczak, and D. A. Shapiro, Proceedings of the National Academy of Sciences **113**, E8219 (2016).
[18] W. Chao, B. D. Harteneck, J. A. Liddle, E. H. Anderson, and D. T. Attwood, Nature **435**, 1210 (2005).
[19] Y. Jiang, Z. Chen, Y. Han, P. Deb, H. Gao, S. Xie, P. Purohit, M. W. Tate, J. Park, S. M. Gruner, *et al.*, Nature **559**, 343 (2018).
[20] K. van Benthem, A. R. Lupini, M. P. Oxley, S. D. Findlay, L. J. Allen, and S. J. Pennycook, Ultramicroscopy **106**, 1062 (2006).
[21] A. Y. Borisevich, A. R. Lupini, and S. J. Pennycook, Proceedings of the National Academy of Sciences **103**, 3044 (2006).
[22] G. Behan, E. Cosgriff, A. I. Kirkland, and P. D. Nellist, Philosophical Transactions of the Royal Society A: Mathematical, Physical and Engineering Sciences **367**, 3825 (2009).
[23] P. D. Nellist, Materials Science in Semiconductor Processing **65**, 18 (2017).
[24] R. Ishikawa, S. J. Pennycook, A. R. Lupini, S. D. Findlay, N. Shibata, and Y. Ikuhara, Applied Physics Letters **109**, 163102 (2016).
[25] T. J. Pennycook, H. Yang, L. Jones, M. Cabero, A. Rivera-Calzada, C. Leon, M. Varela, J. Santamaria, and P. D. Nellist, Ultramicroscopy **174**, 27 (2017).
[26] K. van Benthem, A. R. Lupini, M. Kim, H. S. Baik, S. Doh, J.-H. Lee, M. P. Oxley, S. D. Findlay, L. J. Allen, J. T. Luck, *et al.*, Applied Physics Letters **87**, 034104 (2005).
[27] H. Yang, J. Lozano, T. Pennycook, L. Jones, P. Hirsch,

and P. Nellist, Nature Communications **6**, 7266 (2015).
[28] H. L. Xin and D. A. Muller, Microscopy and Microanalysis **16**, 445 (2010).
[29] G. Saito, F. Yamaki, Y. Kunisada, N. Sakaguchi, and T. Akiyama, Ultramicroscopy **175**, 97 (2017).
[30] J. Hwang, J. Y. Zhang, A. J. DAlfonso, L. J. Allen, and S. Stemmer, Physical Review Letters **111**, 266101 (2013).
[31] C. Kisielowski, B. Freitag, M. Bischoff, H. Van Lin, S. Lazar, G. Knippels, P. Tiemeijer, M. van der Stam, S. von Harrach, M. Stekelenburg, *et al.*, Microscopy and Microanalysis **14**, 469 (2008).
[32] P. Schattschneider, S. Rubino, C. Hébert, J. Rusz, J. Kuneš, P. Novák, E. Carlino, M. Fabrizioli, G. Panaccione, and G. Rossi, Nature **441**, 486 (2006).
[33] P. Schattschneider, M. Stöger-Pollach, S. Rubino, M. Sperl, C. Hurm, J. Zweck, and J. Rusz, Physical Review B **78**, 104413 (2008).
[34] P. Schattschneider, C. Hébert, S. Rubino, M. Stöger-Pollach, J. Rusz, and P. Novák, Ultramicroscopy **108**, 433 (2008).
[35] S. Muto, J. Rusz, K. Tatsumi, R. Adam, S. Arai, V. Kocevski, P. M. Oppeneer, D. E. Bürgler, and C. M. Schneider, Nature Communications **5**, 3138 (2014).
[36] T. Thersleff, J. Rusz, S. Rubino, B. Hjörvarsson, Y. Ito, N. J. Zaluzec, and K. Leifer, Scientific Reports **5**, 13012 (2015).
[37] D. Song, A. H. Tavabi, Z.-A. Li, A. Kovács, J. Rusz, W. Huang, G. Richter, R. E. Dunin-Borkowski, and J. Zhu, Nature Communications **8** (2017).
[38] J. Rusz, S. Rubino, O. Eriksson, P. M. Oppeneer, and K. Leifer, Physical Review B **84**, 064444 (2011).
[39] B. Loukya, X. Zhang, A. Gupta, and R. Datta, Journal of Magnetism and Magnetic Materials **324**, 3754 (2012).
[40] B. Loukya, D. Negi, K. Dileep, N. Pachauri, A. Gupta, and R. Datta, Physical Review B **91**, 134412 (2015).
[41] D. Negi, B. Loukya, and R. Datta, Applied Physics Letters **107**, 232404 (2015).
[42] J. Rusz, O. Eriksson, P. Novák, and P. M. Oppeneer, Physical Review B **76**, 060408 (2007).
[43] L. Calmels, F. Houdellier, B. Warot-Fonrose, C. Gatel, M. Hÿtch, V. Serin, E. Snoeck, and P. Schattschneider, Physical Review B **76**, 060409 (2007).
[44] J. Rusz, J.-C. Idrobo, and S. Bhowmick, Physical Review Letters **113**, 145501 (2014).
[45] Z. Wang, A. H. Tavabi, L. Jin, J. Rusz, D. Tyutyunnikov, H. Jiang, Y. Moritomo, J. Mayer, R. E. Dunin-Borkowski, R. Yu, *et al.*, Nature Materials **17**, 221 (2018).
[46] D. Negi, J. Spiegelberg, S. Muto, T. Thersleff, M. Ohtsuka, L. Schönström, K. Tatsumi, and J. Rusz, Physical Review Letters **122**, 037201 (2019).
[47] A. J. D' Alfonso, S. D. Findlay, M. P. Oxley, S. J. Pennycook, K. van Benthem, and L. J. Allen, Ultramicroscopy **108**, 17 (2007).
[48] P. Wang, G. Behan, M. Takeguchi, A. Hashimoto, K. Mitsuishi, M. Shimojo, A. I. Kirkland, and P. D. Nellist, Physical Review Letters **104**, 200801 (2010).
[49] D. S. Negi, J. C. Idrobo, and J. Rusz, Scientific Reports **8**, 4019 (2018).
[50] M. Uchida and A. Tonomura, Nature **464**, 737 (2010).
[51] J. Verbeeck, H. Tian, and P. Schattschneider, Nature **467**, 301 (2010).
[52] B. J. McMorran, A. Agrawal, I. M. Anderson, A. A. Herzing, H. J. Lezec, J. J. McClelland, and J. Unguris, Science **331**, 192 (2011).
[53] K. Bliokh, I. Ivanov, G. Guzzinati, L. Clark, R. Van Boxem, A. Béché, R. Juchtmans, M. Alonso, P. Schattschneider, F. Nori, *et al.*, Physics Reports **690**, 1 (2017).
[54] H. Ali, T. Warnatz, L. Xie, B. Hjörvarsson, and K. Leifer, Ultramicroscopy **196**, 192 (2019).
[55] O. L. Krivanek, T. C. Lovejoy, N. Dellby, T. Aoki, R. Carpenter, P. Rez, E. Soignard, J. Zhu, P. E. Batson, M. J. Lagos, *et al.*, Nature **514**, 209 (2014).
[56] R. Erni, M. D. Rossell, C. Kisielowski, and U. Dahmen, Physical Review Letters **102**, 096101 (2009).
[57] J. Rusz, S. Bhowmick, M. Eriksson, and N. Karlsson, Physical Review B **89**, 134428 (2014).
[58] J. Rusz, Ultramicroscopy **177**, 20 (2017).
[59] H. Kohl and H. Rose, Advances in Electronics and Electron Physics **65**, 173 (1985).
[60] J. Rusz, H. Lidbaum, S. Rubino, B. Hjörvarsson, P. M. Oppeneer, O. Eriksson, and K. Leifer, Physical Review B **83**, 132402 (2011).
[61] A. Ankudinov and J. Rehr, Phys. Rev. B **51**, 1282 (1995).
[62] O. L. Krivanek, M. F. Chisholm, N. Dellby, and M. F. Murfitt, in *Scanning Transmission Electron Microscopy*, edited by S. J. Pennycook and P. D. Nellist (Springer, 2011) Chap. 15, pp. 615–658.
[63] A. Blackburn and J. Loudon, Ultramicroscopy **136**, 127 (2014).
[64] A. Béché, R. V. Boxem, G. V. Tendeloo, and J. Verbeeck, Nature Physics **10**, 26 (2014).
[65] G. Guzzinati, L. Clark, A. Bch, R. Juchtmans, R. V. Boxem, M. Mazilu, and J. Verbeeck, Ultramicroscopy **151**, 85 (2015), special Issue: 80th Birthday of Harald Rose; PICO 2015 Third Conference on Frontiers of Aberration Corrected Electron Microscopy.
[66] P. Blaha, K. Schwarz, G. Madsen, D. Kvasnicka, J. Luitz, R. Laskowski, F. Tran, and L. Marks, *WIEN2k* (2001).
[67] H. Sawada, Y. Tanishiro, N. Ohashi, T. Tomita, F. Hosokawa, T. Kaneyama, Y. Kondo, and K. Takayanagi, Journal of Electron Microscopy **58**, 357 (2009).
[68] J. Rusz, D. Negi, L. Jones, and J.-C. Idrobo, Microscopy and Microanalysis **24**, 918 (2018).
[69] S. Van Aert, A. De Backer, L. Jones, G. T. Martinez, A. Béché, and P. D. Nellist, Physical Review Letters **122**, 066101 (2019).
[70] S. Löffler and W. Hetaba, Microscopy **67**, i60 (2018).
[71] J. Rusz and J. C. Idrobo, Phys. Rev. B **93**, 104420 (2016).
[72] L. Jones, H. Yang, T. J. Pennycook, M. S. J. Marshall, S. Van Aert, N. D. Browning, M. R. Castell, and P. D. Nellist, Advanced Structural and Chemical Imaging **1**, 8 (2015).
[73] J. Spiegelberg, J. Rusz, and K. Pelckmans, Ultramicroscopy **175**, 36 (2017).